HHS Public Access

Author manuscript

Cell Rep. Author manuscript; available in PMC 2016 August 11.

Published in final edited form as:

Cell Rep. 2015 August 11; 12(6): 955–964. doi:10.1016/j.celrep.2015.07.018.

Visual Deprivation Causes Refinement of Intracortical Circuits in the Auditory Cortex

Xiangying Meng[1], **Joseph P.Y. Kao**[2], **Hey-Kyoung Lee**[1,3], and **Patrick O. Kanold**[1,*]

[1]Department of Biology, University of Maryland, College Park, MD 20742, USA

[2]Center for Biomedical Engineering and Technology and Department of Physiology, University of Maryland School of Medicine, Baltimore, MD 21201, USA

[3]Department of Neuroscience, Mind/Brain Institute, Johns Hopkins University, Baltimore, MD 21218, USA

SUMMARY

Loss of a sensory modality can lead to functional enhancement of the remaining senses. For example, short-term visual deprivations, or dark exposure (DE), can enhance neuronal responses in the auditory cortex to sounds. These enhancements encompass increased spiking rates and frequency selectivity as well as increased spiking reliability. Although we previously demonstrated enhanced thalamocortical transmission after DE, increased synaptic strength cannot account for increased frequency selectivity or reliability. We thus investigated whether other changes in the underlying circuitry contributed to improved neuronal responses. We show that DE can lead to refinement of intra- and inter-laminar connections in the mouse auditory cortex. Moreover, we use a computational model to show that the combination of increased transmission and circuit refinement can lead to increased firing reliability. Thus cross-modal influences can alter the spectral and temporal processing of sensory stimuli by refinement of thalamocortical and intracortical circuits.

Graphical Abstract

*Correspondence: pkanold@umd.edu.

AUTHOR CONTRIBUTIONS

H.-K.L. and P.O.K. designed research. X.M. performed LSPS experiments and analyzed the data. P.O.K. supervised research. J.P.Y.K. contributed reagents. X.M., H.-K.L., J.P.Y.K., and P.O.K. discussed the results and wrote the manuscript.

SUPPLEMENTAL INFORMATION

Supplemental Information includes three figures and can be found with this article online at http://dx.doi.org/10.1016/j.celrep.2015.07.018.

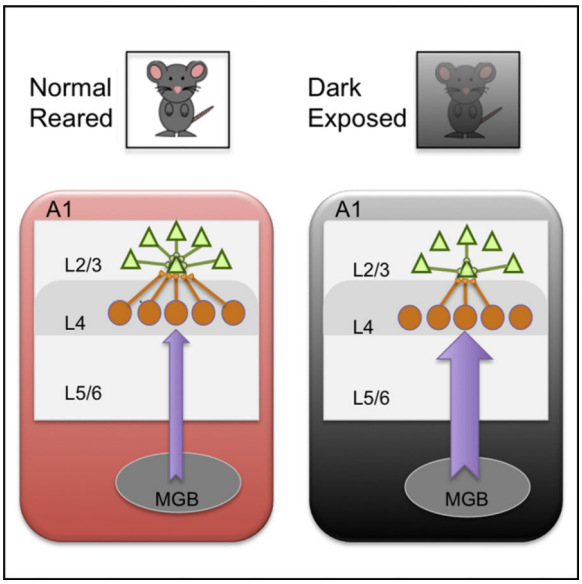

INTRODUCTION

The loss of a sensory modality can lead to functional enhancement of the remaining senses in a process often termed “cross-modal plasticity” (Bavelier and Neville, 2002). For example, blind individuals can display better tactile acuity (Grant et al., 2000; Van Boven et al., 2000; Goldreich and Kanics, 2003), sound localization (Lessard et al., 1998; Röder et al., 1999), and pitch discrimination (Gougoux et al., 2004) than sighted individuals. These results suggest that the absence of vision may trigger a refinement and/or sharpening of the remaining senses. There is accumulating evidence that even primary sensory cortices receive subthreshold modulatory information from other sensory systems. These inputs are thought important for multi-sensory integration under normal conditions (Schroeder and Foxe, 2005; Ghazanfar and Schroeder, 2006) and mainly activate the superficial layers of a primary sensory cortex (Lakatos et al., 2007; Iurilli et al., 2012).

We recently showed that depriving mice of vision by dark exposure (DE) for about 1 week alters the sound-evoked responses in layer 4 (L4) of primary auditory cortex (A1) in that cells responded more robustly to sounds but also showed increased frequency selectivity (Petrus et al., 2014). Whereas some of these changes in the responsiveness to sound can be attributed to increased thalamocortical transmission following DE (Petrus et al., 2014), increased frequency selectivity and spiking reliability cannot be accounted for by increased gain at the thalamo-cortical synapse but likely requires refinement of thalamocortical as well as intracortical excitatory or inhibitory synapses, which can alter the spectral tuning of A1 cells (Li et al., 2013, 2014). DE also causes changes to miniature excitatory postsynaptic current (mEPSC) amplitudes in the superficial layers in A1 as well as in primary somatosensory cortex (S1) (Goel et al., 2006; He et al., 2012). Layer 2/3 (L2/3) neurons receive excitatory and inhibitory inputs from the superficial and granular layers, and refinement of these connections can give rise to increased frequency selectivity. We therefore investigated whether DE causes a refinement of intracortical circuits in A1.

Although mEPSC and miniature inhibitory postsynaptic current (mIPSC) recordings enable an investigation of changes in the strength of individual synapses onto a neuron, they do not reveal which synapses are affected. Moreover, changes in synapse numbers between cells or the strength of unitary connections will not be revealed. Thus, to identify which microcircuits in A1 are affected by visual experience, we here use laser-scanning photostimulation (LSPS) to spatially map the connectivity of excitatory and inhibitory inputs to A1 neurons to determine whether visual deprivation alters their circuit topology. To assess changes in both intra- and inter-laminar connections, we record from L2/3 neurons. We find that 6–8 days of dark rearing does not affect the intrinsic excitability of L2/3 neurons but does alter the spatial pattern of both excitatory and inhibitory intra- and inter-laminar connections. Moreover, our results indicated that, in general, inter-laminar excitatory inputs originating from L4 were confined to a smaller area, indicating refinement of ascending connections. Furthermore, inhibitory inputs were also refined. To investigate the effects of circuit refinement, we implemented a computational model and found that refinement also resulted in more-reliable responses. Together, our results show that DE can refine the intracortical circuits in A1 to facilitate enhanced spectro-temporal processing of sound stimuli.

RESULTS

We use LSPS of caged glutamate (Shepherd et al., 2003; Meng et al., 2014) to spatially map the connectivity of excitatory and inhibitory inputs to A1 neurons (n = 102 cells) to determine whether visual deprivation alters the circuit in A1.

Intrinsic Excitability of Cells in A1 Is Unchanged after DE

Because manipulations in sensory experience might alter the intrinsic excitability of neurons, we tested whether indeed DE could lead to altered excitability of A1 neurons. We performed current clamp recordings of A1 neurons from DE and normal reared (NR) animals. Recorded cells were obtained from a similar region within L2/3 (Figures 1A and 1B). Using current injections of various amplitudes normalized to rheobase and plotting the resulting action potential number, we find that the two groups have comparable excitability (Figure S1). Next, we investigate whether the spatial expression of glutamate receptors (GluRs) on the soma and dendrites of A1 neurons is altered after DE so as to change the area from which action potentials are evoked. We performed cell-attached patch recordings from cells in L2/3 and L4 of A1 combined with LSPS in DE and NR animals. We target short UV laser pulses to multiple distinct stimulus locations. The UV light focally releases glutamate, which activates neurons located under the beam to fire action potentials. Owing to the small size (≤20 μm) of the focused laser spot, the spatial resolution of this technique is quite high. The stimulus locations span the entire extent of the cortex, which enables us to “map” the entire 2D activation pattern of a given cell. We measured the area and the maximal extent within which short-latency (<50 ms) action potentials were evoked. We find that, in both DE and NR animals, most (>80%) action potentials were generated when the stimulation spot was targeted to within 100 μm of the soma (Figure 1C). The area from which action potentials could be evoked was unchanged after DE in L2/3 and L4 (L2/3: $p = 0.928$; L4: $p = 0.890$; KS test), and the numbers of action potentials evoked also stayed the same (L2/3: p

= 0.731; L4: p = 0.660; Figure 1D). These findings suggest that DE does not cause increased excitability or an increased sensitivity of L4 and L2/3 cells to gluta-mate (e.g., by redistribution of GluRs to the soma or proximal dendrites).

Intra- and Inter-laminar Excitatory Connections in A1 Change after DE

Next, we investigated whether the spatial pattern of intra- and inter-laminar connectivity is altered after DE. To map the spatial pattern of excitatory inputs to a given cell, we perform whole-cell patch recordings at a holding potential of –70 mV (~E_{Cl}). We then target the laser pulse to multiple distinct stimulus locations and record the resulting membrane currents (Figure 1E). Whereas synaptic currents have a distinct latency (>8 ms), activation of the cell body and proximal dendrites causes a large-amplitude short-latency direct event (Figure S1). The stimulus locations span the entire extent of the cortex, thus enabling us to map the entire 2D connection pattern of excitatory inputs to a given cell (Figure 1A). If the activated neuron under the laser beam is connected to the recorded neuron, then EPSCs are observed (Figure 1E).

We mapped 102 cells in A1 and investigated the connection pattern of excitatory inputs. For cells in NR animals, the spatial patterns of intracortical excitatory inputs could be diverse (Figure 1F). To analyze the changes in the connectivity pattern over the population of cells, individual LSPS maps were aligned to the cell body position and averaged; the result is a spatial map of connection probability (Figure 2A) and the average connection strength (Figure 2B). Altered synaptic connectivity can be manifested as altered occurrence of connections as well as changes in the strength of existing connections. We thus analyze the spatial connection probability and the spatial connection strength separately.

When qualitatively comparing NR to DE, we find that, after DE, there are distinct differences in excitatory inputs to L2/3 neurons (Figures 2A and 2B). Overall, there seems to be a reduction in connection probability as well as in total EPSC charge for inputs originating from L2/3 and L4. Whereas average connection maps allow a coarse assessment of changes, detailed changes in connection profiles cannot be extracted because the individual connection profiles are diverse (Figure 1F). We thus analyzed properties of the connection patterns for each individual cell in detail and then compared these properties over the population. To quantify the laminar changes, we identified laminar borders for each cell from the DIC images and calculated the input profile from each layer. To visualize and quantify the differences between cells, we determined the total area in each layer where stimulation evoked EPSCs in L2/3 neurons. We find that, after DE, excitatory inputs originate from smaller areas in L4 as well as L2/3—suggesting a pruning/refinement of functional connections (Figure 2C).

Next, we investigated the amplitude of events evoked from each layer. We find that the mean peak EPSC amplitude and mean integrated charge of events originating from L4 and L2/3 were similar (Figure 2D). To further quantify the laminar changes, we also calculated the distributions of uncaging evoked EPSC amplitude and charge from each layer (Figure S2). We find that the distributions were similar, although there was a trend for reduced input from L4 (p = 0.062), which suggests possible re-weighting of input to L2/3 neurons.

Together, our analyses show a refinement of inter- and intra-laminar connections to L2/3 neurons after DE.

Intra- and Inter-laminar Inhibitory Connections in A1 Change after DE

Our results show a substantial remodeling of excitatory connections. Next, we investigated whether inhibitory connections also change after DE. We map inhibitory connections by holding cells at 0 mV (~E_{glut}; Figures 1E and 1F). Average maps of connection probability and connection strength appeared different after DE in that the cortical area giving rise to inhibitory responses decreased (Figures 3A and 3B). Quantification of the laminar inputs confirmed this: the total area generating input as well as total input from all layers was reduced after DE compared to NR controls (Figure 3C). In contrast, the average amplitude of un-caging evoked IPSC was unchanged (Figure 3D). Calculating the fractional input from each layer showed that cells received identical percentages of input from the cortical layers (Figure S3), suggesting that the relative contribution of intra-laminar and inter-laminar connections was unchanged after DE. Notice that the inhibitory inputs from L5/6 show significant decrease after DE, whereas the reduction of excitatory inputs from L5/6 was not significant. This could be due to the larger heterogeneity of excitatory L5/6 inputs to L2/3 neurons. Taken together, the above results demonstrate refinement of both excitatory and inhibitory connections after DE.

The Balance of Excitation and Inhibition in A1 Does Not Change after DE

Our results show a substantial remodeling of excitatory and inhibitory connections. The balance of excitation and inhibition is crucial for sensory processing (Li et al., 2013, 2014). We thus investigated whether the changes in the spatial pattern of excitatory and inhibitory connection co-vary. We thus computed the excitation/inhibition (EI) ratio based on transferred charge, peak amplitude, or area for every cell. We excluded stimulus locations for quantifying inhibition that were giving direct responses for excitation because we could not assess excitatory input there. Our calculations showed that this EI ratio was not changed after DE (Figure 4). Thus, the spatial patterns of excitatory and inhibitory inputs co-vary.

A Computational Model Reveals Circuit Changes Can Increase Reliability of Sound-Evoked Responses after DE

Our results so far show that A1 circuits refine, consistent with the observed increase in frequency selectivity following DE (Petrus et al., 2014). Because cells also responded more reliably to sounds after DE, we asked whether the observed circuit refinement could underlie the observed increase in reliability. We implemented a simple computational network model to shed light on how circuit modifications in ACX can enhance the processing of sensory stimuli. The model comprises two layers corresponding to L4 and L2/3 (Figure 5A). The input stage of this model is L4. Reflecting the topologically organized frequency-based (tonotopic) axis in the A1, L4 is constructed with 12 frequency-selective units with frequency bands changing in a stepwise logarithmic fashion (Figures 5A1 and 5B1). The total frequency range is 2–80 kHz, covering the most-salient part of the dynamic range of the mouse auditory spectrum (Figures 5A1 and 5B1). Each unit contains neurons with their characteristic frequency (CF), which is the same as the unit frequency. For each sound level,

each neuron has a Gaussian-shaped frequency-receptive field with center at CF. Receptive field width is positively correlated to sound level (see Experimental Procedures Equation 1). Figures 5B1 and 5B2 show the receptive field for a neuron with CF of 30 kHz. The parameters were chosen to match the observed changes in firing rates after DE (Petrus et al., 2014). L4 neurons receive thalamic input, and their firing rates are modulated by the amplitude of the sound. We thus mimic the evoked responses of L4 neurons corresponding to sinusoidal amplitude-modulated (SAM) tone stimuli with independent time-varying Poisson spike trains. Each L4 neuron also has a spontaneous firing rate of 2 Hz, which is modeled by a uniform Poisson process. The firing probability for each L4 neuron follows the amplitude modulation of the rectified SAM stimulus (Figure 5C, traces labeled FR). Each unit in L2/3 receives inputs from L4 neurons as well as a variety of other inputs such as from other L2/3 cells. We modeled all these other sources of inputs to L2/3 neurons simply with an 8-Hz uniform Poisson process. L2/3 units are modeled as integrate-and-fire neurons. The parameters in the model were chosen so that the properties of L2/3 neurons resemble those found in the regular spiking neurons in L3 of the A1 in the juvenile mouse (Rose and Metherate, 2005). Because our experimental results showed that DE alters the number of input sources from L4 to L2/3 as well as the TC connection strengths, in the simulation, we only explore those two parameters across a large parameter domain but keep all the other parameters unchanged.

In the DE case, the number of the input sources to L2/3 units is reduced and the firing rate of L4 neurons is enhanced. Figures 5C and 5D1–5D3 show an example of the two-parameter sets for the NR and DE cases, respectively. The maximum firing rate of the L4 neurons corresponding to 60 dB pure tone stimulus is 50 Hz in the NR case and 100 Hz in the DE case. And the number of connections from each column in L4 is 40 in the NR case and 20 in the DE case (Figure 5F, black stars). We computed the membrane potential (V_m) in L2/3 neurons (Figure 5C, right traces). We observed that, in the NR control, V_m crossed the firing threshold of the L2/3 neuron (dashed horizontal line) at various times both within and outside the interval of the sound stimulus, which indicates poor tracking of the SAM envelope by the L2/3 spikes. To measure the quality of encoding the SAM tone, we first calculated the post-stimulus time histogram (PSTH) of L2/3 neurons (Figures 5D1–5D3). To quantify the temporal precision of L2/3 activity, we then calculated the vector strength of the PSTH for each L2/3 cell (see the Supplemental Information for details of calculation). The vector strength is a metric to quantify phase locking or an increase in spike discharge rate at a certain phase of the stimulus. To identify changes in firing reliability over a range of modulation frequencies, we varied the SAM frequency and calculated the vector strength for a wide range of SAM-modulation frequencies. We observed that vector strength, and thus reliability, decreased as the modulation frequency increased (Figure 5E).

Next, we investigated whether the circuit changes after DE altered the responses to SAM stimuli. Because after DE, the connection strength from MGB to L4 neurons is strengthened, leading to higher evoked responses of L4 neurons (Petrus et al., 2014), we increased the maximal firing rate of L4 neurons in the model (Figures 5A2 and 5B2). Because our results show that excitatory connections between L4 and L2/3 refine (see Figure 2), we reduced the number of inputs from L4 to L2/3 cells in the model. Because our data showed that the average uncaging-evoked EPSC amplitude stayed constant after DE (Figure 2), the

connection strength from L4 to L2/3 was left unchanged. Because DE increases the spontaneous firing rate of L4 neurons in vivo, we also doubled the spontaneous firing rate of L4 neurons in the model in order to investigate whether such increases could affect the reliability of responses to sound stimuli (Figure 5E, dashed lines). After these network changes, we observe that, compared to the NR condition, action potentials occur more frequently within the same SAM phase (Figures 5C, right, and 5D1). Calculating the vector strength of the PSTH for each L2/3 cell shows that, after DE, L2/3 neurons show increased vector strength over a wide range of modulation frequencies. The increased spontaneous rate of L4 neurons causes only slight decreases in vector strength (Figure 5E). This indicates that, after DE, L2/3 neurons encode SAM tones more reliably than NR controls at all modulation frequencies (Figure 5E). Next, we investigated the individual effect of thalamocortical connection strength and circuit refinement on the reliability of L2/3 responses. We systematically varied both L4 firing rates and the number of connections between L4 and L2/3 and calculated vector strength for each SAM modulation rate (Figure 5F). We observed that both changes in the numbers of connections and changes in L4 firing rates could increase vector strength. However, the largest increases in vector strength were observed when both were coordinated. Thus, the enhancement in reliability in the temporal responses is due to the combination of the refined connections and the stronger thalamocortical transmission.

DISCUSSION

DE can enhance sound processing in A1 by enhancing responsiveness, increasing frequency selectivity, and increasing firing reliability (Petrus et al., 2014). Such changes in sound-evoked responses are likely due to changes in synaptic strength and refinement of synaptic connections. We previously showed that thalamocortical connections strengthen after DE (Petrus et al., 2014). Here, we investigated whether DE can also lead to refinement of intracortical connections. We show that short-term DE causes a refinement of the functional intracortical circuitry in A1. We find that inter-laminar inputs from L4 and intra-laminar excitatory inputs to L2/3 originate from smaller areas—consistent with a refinement of these connections. Inputs from L5/6 only showed a trend to refined inputs likely due to the heterogeneity of L5/6 projections over the population (see Figure 1F). DE did not only affect excitatory inputs. Ascending inhibitory connections from L4, as well as L5/6 and intra-laminar inputs, also originated from reduced areas. Thus, overall, there is a net decrease in the spatial extent of inhibition to L2/3 cells. These changes in synaptic connectivity pattern were not accompanied by changes in intrinsic excitability of A1 L2/3 cells. These connection changes might underlie changes in frequency selectivity in A1.

In the barrel cortex, the spatial connectivity map is altered by whisker deprivation in that excitatory input from L4 to L2/3 are decreased in above barrel cells and increased in above septal cells (Shepherd et al., 2003). Moreover, intra-laminar connections to L2/3 cells seemed to increase (Shepherd et al., 2003), thus changing the laminar balance of inputs to each cell type. In the present study, we show that cross-modal influences decrease ascending input from L4 and that this is due to a refinement of the connections. We also show that intra-laminar connections from L2/3 also refine, so that overall L2/3 neurons receive the same balance of inputs from each layer, but the input originate from more-restricted areas.

As in our prior studies (Goel et al., 2006; He et al., 2012; Petrus et al., 2014), we performed our visual deprivation on animals within the critical period for V1 plasticity but after the critical period for A1 plasticity (Barkat et al., 2011; Espinosa and Stryker, 2012). Because we have shown that cross-modal synaptic plasticity occurs in adults (Petrus et al., 2014, 2015), the changes observed here are not likely restricted to the V1 critical period.

Our results are consistent with a cross-modal reduction in GluR levels after DE (Goel et al., 2006). However, in contrast to a reduction in mEPSC amplitude after DE (Goel et al., 2006), we do not observe consistent changes in photostimulation-evoked EPSC amplitude (Figure 2). This difference could be due to the fact that our current method measures connection strength, which is a function of the strength of individual synapses and the number of functional connections. Hence, concomitant and opposite changes in individual synaptic strength and the number of functional connections will preserve the net connection strength. Moreover, the spatial resolution of our LSPS technique is ~100 μm due to the direct response. As a result, we cannot measure changes in connections of neurons that are very close by, and it is possible that DE strongly affects these very local connections. In any case, we found that the amplitude of evoked PSCs stays constant after DE. Our measure quantifies the functional strength of connections between cells, which typically involve multiple synapses between a pair of cells. Thus, even though the functional connection strength between cells was constant, individual synaptic contacts might have changed. Our results suggest that the changes after DE include spatial refinement of ascending inputs to A1 L2/3 neurons into fewer synapses, and our modeling shows that such a refinement improves the reliability of neuronal responses even further. Thus, the combined effect of these circuit changes will be enhanced transmission of ascending auditory information. Therefore, DE leads to enhancement of spectro-temporal responses in A1. Because, in A1, L2/3 neurons sample from a large range of frequency bands (Bandyopadhyay et al., 2010; Chen et al., 2011) and because there exists a distinct transformation in frequency representation between L4 and L2/3 (Bandyopadhyay et al., 2010; Rothschild et al., 2010; Winkowski and Kanold, 2013), our data suggest that this plasticity will restrict the frequency range in which L2/3 neurons sample and thereby sharpen the tuning of L2/3 cells.

DE leads to enhanced firing reliability of cortical responses (Petrus et al., 2014). Our computational model suggests that such an enhanced reliability can be achieved by a reduction of the number of L4 neurons sending inputs to L2/3 cells, thus reducing the amount of background “noise” L2/3 cells integrate. However, this reduction would decrease the transmission of ascending information as well. Our calculations show that the increased responsiveness of L4 neurons can compensate for this loss so that the firing threshold of L2/3 neurons will not be increased due to the reduction of connections. Therefore, by combining both mechanisms (refinement and enhanced responses), L2/3 neurons respond to sound stimuli with high signal-to-noise ratio, which represents better sound encoding. Importantly, better sound encoding requires both of these mechanisms. The functional refinement of connectivity without obvious changes in the connection strength between cells may be due to loss of inputs to L2/3 neurons, but we cannot rule out the possibility that it also involves an increase in inhibitory synaptic strength combined with additional refinement of the synaptic connections between pairs of neurons. A balanced increase in both excitatory and inhibitory synaptic strength combined with additional refinement on the

synaptic level could lead to even higher signal to noise and limit the spatial spread of excitation. Indeed, the balance of excitatory and inhibitory synaptic conductances has been shown to be critical for A1 frequency tuning (Wu et al., 2008).

Whereas we observe pronounced changes in the connectivity of A1, it is unclear how these changes come about. There are multiple non-exclusive possibilities. Descending visual input from extrastriate visual cortex is known to modulate A1 (Vakulin et al., 2012). Thus, a reduction in this input could lead to changes in A1. Moreover, tuning of A1 neurons can be altered by attention state, possibly via neuromodulatory or top-down pathways (Kilgard and Merzenich, 1998; Bao et al., 2001; Fritz et al., 2003, 2007; Winkowski et al., 2013). Thus, changes in the attention state of the animal while in the dark could cause plasticity of thalamocortical and intracortical circuits.

Whatever the mechanism underlying the observed changes, the sum of our observations indicates changes in both excitatory and inhibitory connections consequent to DE. Our results thus reveal a powerful effect of cross-modal inputs on the intrinsic circuitry of A1.

EXPERIMENTAL PROCEDURES

Animals

All procedures were approved by the University of Maryland Institutional Animal Care and Use Committee. Male and female C57BL/6J mice (Jackson Laboratories) were raised in 12 hr light/12 hr dark conditions. At P21 to P22, mice (two to three mice from established litters and single gender per cage) were dark exposed (DE) for 6–8 days. Age-matched controls remained in normal light conditions (NR).

Slice Preparation

Mice are deeply anesthetized with isoflurane (Halocarbon). A block of brain containing A1 and the medial geniculate nucleus (MGN) is removed and thalamocortical slices (500 μm thick) are cut on a vibrating microtome (Leica) in ice-cold ACSF containing (in mM) 130 NaCl, 3 KCl, 1.25 KH_2PO_4, 20 $NaHCO_3$, 10 glucose, 1.3 $MgSO_4$, and 2.5 $CaCl_2$ (pH 7.35–7.4; in 95%O_2-5%CO_2). For A1 slices, the cutting angle is ~15 degrees from the horizontal plane (lateral raised; Cruikshank et al., 2002; Zhao et al., 2009). Slices are incubated for 1 hr in ACSF at 30° C and then kept at room temperature. For recording, slices are held in a chamber on a fixed-stage microscope (Olympus BX51) and superfused (2–4 ml/min) with high-Mg ACSF recording solution at room temperature to reduce spontaneous activity in the slice. The recording solution contained (in mM) 124 NaCl, 5 KCl, 1.23 NaH_2PO_4, 26 $NaHCO_3$, 10 glucose, 4 $MgCl_2$, and 4 $CaCl_2$. The location of the recording site in A1 was identified by landmarks (Cruikshank et al., 2002; Zhao et al., 2009).

Electrophysiology

Whole-cell recordings are performed with a patch clamp amplifier (Multiclamp 700B; Axon Instruments) using pipettes with input resistance of 4–9 MΩ. Data acquisition is performed by National Instruments AD boards and custom software (Ephus; Suter et al., 2010). Ephus is written in MATLAB (Mathworks) and adapted to our setup. Voltages were corrected for

an estimated junction potential of 10 mV. Electrodes are filled with (in mM) 115 cesium methanesulfonate ($CsCH_3SO_3$), 5 NaF, 10 EGTA, 10 HEPES, 15 CsCl, 3.5 MgATP, and 3 QX-314 (pH 7.25; 300 mOsm). Biocytin or Neurobiotin (0.5%) is added to the electrode solution as needed. Series resistances were typically 20–25 MΩ.

Photostimulation—0.5–1 mM caged glutamate (*N*-(6-nitro-7-coumarylmethyl)-L-glutamate; Ncm-Glu; Kao, 2006) is added to the ACSF. Without UV light, this compound has no effect on neuronal activity (Kao, 2006). UV laser light (500 mW, 355 nm, 1-ms pulses; 100 kHz repetition rate; DPSS) is split by a 33% beam splitter (CVI Melles Griot), attenuated by a Pockels cell (Conoptics), gated with a laser shutter (NM Laser), and coupled into a microscope via scan mirrors (Cambridge Technology) and a dichroic mirror. The laser beam in LSPS enters the slice axially through the objective (Olympus 10×; 0.3 NA/water) and has a diameter of <20 μm. Laser power at the sample is <25 mW. We typically stimulated up to 40 × 35 sites spaced 30 μm apart, enabling us to probe areas of 1 mm^2; such dense sampling reduces the influence of potential spontaneous events. Repeated stimulation yielded essentially identical maps. Stimuli are applied at 0.5–1Hz. Analysis was performed essentially as described previously (Meng et al., 2014) with custom software written in MATLAB. Activation profiles of neurons were produced by recording in cell-attached mode while mapping the same region and recording action potentials. To detect monosynaptically evoked PSCs, we detected PSCs with onsets in an approximately 50-ms window after the stimulation. This window was chosen based on the observed spiking latency under our recording conditions (Figure 1D). Our recordings are performed at room temperature and in high-Mg^{2+} solution to reduce the probability of multisynaptic inputs. We measured both peak amplitude and transferred charge; transferred charge was measured by integrating the PSC. Whereas the transferred charge might include contributions from multiple events, our prior studies showed a strong correlation between these measures (Viswanathan et al., 2012; Meng et al., 2014). Traces containing a short-latency (<8 ms) “direct” response (Figure 1F) were discarded from the analysis (black patches in color-coded maps) as were traces that contained longer latency inward currents of long duration (>50 ms). These currents could sometimes be seen in locations surrounding (<100 μm) areas that gave a direct response. Occasionally, some of the direct responses contained synaptic evoked responses that we did not separate out, leading to an underestimation of local short-range connections. Cells that did not show any large (>100 pA) direct responses were excluded from the analysis as these could reflect astrocytes. It is likely that the observed PSCs at each stimulus location represent the activity of multiple presynaptic cells. Layer boundaries were determined from the infrared pictures.

Computational Model

A computational model was implemented in MATLAB (see Figure 5A). The model contains two layers: L4 and L2/3. The input stage of this model is L4. Considering topologically organized frequency-based (tonotopic) axis in the A1, L4 is constructed with 12 frequency selective units with frequency bands changing in a stepwise logarithmic fashion (Figures 5A1 and 5B1). All the neurons inside each unit have the same CF as the unit frequency. Each neuron has Gaussian-shaped receptive field with centers at CF and different standard

variance positively correlated to sound level, i.e., the firing rate function for the neuron in the unit corresponding to the pure tone with frequency f and sound level A is

$$R(f, A, fc) = R_{max} \bullet \rho \bullet e^{\left(-\frac{(f-fc)^2}{2(\sigma_{max}\bullet\rho)^2}\right)}, \quad \text{(Equation 1)}$$

where $\rho = A/60$ and R_{max} is the maximum firing rate for the neuron corresponding to 60-DB sound pressure level (SPL) pure tones at CF.

The activities of all the neurons in L4 were generated by a time-varying Poisson process. The rate of the Poisson process depends on the oscillation of sound level. Specifically, we applied rectified SAM sound to our model (Figure 5), i.e., the modulation wave,

$$A(t) = \begin{cases} \mathrm{A}_{max} \bullet sin(2\pi f_{mod} t), & if\ sin(2\pi f_{mod} t) > 0 \\ 0, & otherwise \end{cases}, \quad \text{(Equation 2)}$$

where A_{max} is the maximum sound level and f_{mod} is the modulation frequency. The envelope of the firing rate $R(t)$ for each neuron at time t also has the same shape as the SAM,

$$R(t) = \begin{cases} R_{max} \bullet sin(2\pi f_{mod} t) + R_{spt}, & if\ sin(2\pi f_{mod} t) > 0 \\ R_{spt}, & otherwise \end{cases}, \quad \text{(Equation 3)}$$

where R_{max} is the maximum firing rate when the sound level is maximum and R_{spt} is the spontaneous rate.

L2/3 units are modeled as integrate-and-fire neurons (Equation 4). Integrating all the individual evoked synaptic currents generates the membrane potential of L2/3 neurons, which fire an action potential when threshold (–20 mV) is reached. Each L2/3 neuron receives multiple synaptic inputs from L4 (I_{syn}) and a variety of other inputs, e.g., from other L2/3 cells. We mimicked these other sources of inputs to L2/3 neurons with an 8-Hz uniform Poisson process. Each L2/3 neuron has a leak current I_{lk} (Equation 5)

$$c_m \frac{dV}{dt} = -I_{lk} + I_{syn} \quad \text{(Equation 4)}$$

$$I_{lk} = G_{lk} \bullet (V - V_0). \quad \text{(Equation 5)}$$

The leak current has conductance G_{lk} = 5 nS, membrane capacitance c_m = 100 pF, and a reversal potential V_0 = –60 mV. The parameters were chosen so that the intrinsic properties of L2/3 neurons resemble those found in the regular spiking neuronsin L3 of the A1 in the juvenile mouse (Rose and Metherate, 2005).

I_{syn} is the postsynaptic current and is calculated from the synaptic evoked conductance changes (EPSG) (Equation 6). Synaptic events are modeled as alpha functions (Equation 6).

$$I_{syn = EPSG \bullet (E_{rev} - V)} \quad \text{(Equation 6)}$$

The excitatory synaptic current has a reversal potential E_{rev} = 0 mV.

$$EPSG = G_{syn} \bullet \frac{t}{\tau} \bullet e^{(1-t/\tau)} \quad \text{(Equation 7)}$$

Each synapse has a postsynaptic conductance of G_{syn} = 16 nS and a synaptic time constant of τ = 6 ms.

Vector strength is a metric to quantify phase locking or an increase in spike discharge rate at a certain phase of the reference stimulus. It is calculated as

$$VS = \frac{1}{N}\sum_{j=1}^{N} e^{(i2\pi f_{mod} t_j)}, \quad \text{(Equation 8)}$$

where t_j is the timing of the j-th spike and f_{mod} is the stimulus frequency.

Statistics

Results are plotted as means ± SD unless otherwise indicated. Populations are compared with a rank sum or Student's t test (based on Lilliefors test for normality), and the PSTH variance comparison is done with F test and deemed significant if $p < 0.05$.

Supplementary Material

Refer to Web version on PubMed Central for supplementary material.

ACKNOWLEDGMENTS

We thank Dr. Kaiwen He for performing preliminary experiments. This work is supported by NIH R01EY022720 (to H.-K.L. and P.O.K.) and NIH R01 GM056481 (to J.P.Y.K.).

REFERENCES

Bandyopadhyay S, Shamma SA, Kanold PO. Dichotomy of functional organization in the mouse auditory cortex. Nat. Neurosci. 2010; 13:361–368. [PubMed: 20118924]

Bao S, Chan VT, Merzenich MM. Cortical remodelling induced by activity of ventral tegmental dopamine neurons. Nature. 2001; 412:79–83. [PubMed: 11452310]

Barkat TR, Polley DB, Hensch TK. A critical period for auditory thalamocortical connectivity. Nat. Neurosci. 2011; 14:1189–1194. [PubMed: 21804538]

Bavelier D, Neville HJ. Cross-modal plasticity: where and how? Nat. Rev. Neurosci. 2002; 3:443–452. [PubMed: 12042879]

Chen X, Leischner U, Rochefort NL, Nelken I, Konnerth A. Functional mapping of single spines in cortical neurons in vivo. Nature. 2011; 475:501–505. [PubMed: 21706031]

Cruikshank SJ, Rose HJ, Metherate R. Auditory thalamocortical synaptic transmission in vitro. J. Neurophysiol. 2002; 87:361–384. [PubMed: 11784756]

Espinosa JS, Stryker MP. Development and plasticity of the primary visual cortex. Neuron. 2012; 75:230–249. [PubMed: 22841309]

Fritz J, Shamma S, Elhilali M, Klein D. Rapid task-related plasticity of spectrotemporal receptive fields in primary auditory cortex. Nat. Neurosci. 2003; 6:1216–1223. [PubMed: 14583754]

Fritz JB, Elhilali M, David SV, Shamma SA. Auditory attention–focusing the searchlight on sound. Curr. Opin. Neurobiol. 2007; 17:437–455. [PubMed: 17714933]

Ghazanfar AA, Schroeder CE. Is neocortex essentially multisensory? Trends Cogn. Sci. 2006; 10:278–285. [PubMed: 16713325]

Goel A, Jiang B, Xu LW, Song L, Kirkwood A, Lee HK. Cross-modal regulation of synaptic AMPA receptors in primary sensory cortices by visual experience. Nat. Neurosci. 2006; 9:1001–1003. [PubMed: 16819524]

Goldreich D, Kanics IM. Tactile acuity is enhanced in blindness. J. Neurosci. 2003; 23:3439–3445. [PubMed: 12716952]

Gougoux F, Lepore F, Lassonde M, Voss P, Zatorre RJ, Belin P. Neuropsychology: pitch discrimination in the early blind. Nature. 2004; 430:309. [PubMed: 15254527]

Grant AC, Thiagarajah MC, Sathian K. Tactile perception in blind Braille readers: a psychophysical study of acuity and hyperacuity using gratings and dot patterns. Percept. Psychophys. 2000; 62:301–312. [PubMed: 10723209]

He K, Petrus E, Gammon N, Lee HK. Distinct sensory requirements for unimodal and cross-modal homeostatic synaptic plasticity. J. Neurosci. 2012; 32:8469–8474. [PubMed: 22723686]

Iurilli G, Ghezzi D, Olcese U, Lassi G, Nazzaro C, Tonini R, Tucci V, Benfenati F, Medini P. Sound-driven synaptic inhibition in primary visual cortex. Neuron. 2012; 73:814–828. [PubMed: 22365553]

Kao, JPY. Caged molecules: principles and practical considerations.. In: Gerfen, C.; Holmes, A.; Rogawski, M.; Sibley, D.; Skolnick, P.; Wray, S., editors. Current Protocols in Neuroscience. Wiley; Hoboken, NJ: 2006.

Kilgard MP, Merzenich MM. Cortical map reorganization enabled by nucleus basalis activity. Science. 1998; 279:1714–1718. [PubMed: 9497289]

Lakatos P, Chen CM, O'Connell MN, Mills A, Schroeder CE. Neuronal oscillations and multisensory interaction in primary auditory cortex. Neuron. 2007; 53:279–292. [PubMed: 17224408]

Lessard N, Paré M, Lepore F, Lassonde M. Early-blind human subjects localize sound sources better than sighted subjects. Nature. 1998; 395:278–280. [PubMed: 9751055]

Li LY, Li YT, Zhou M, Tao HW, Zhang LI. Intracortical multiplication of thalamocortical signals in mouse auditory cortex. Nat. Neurosci. 2013; 16:1179–1181. [PubMed: 23933752]

Li LY, Ji XY, Liang F, Li YT, Xiao Z, Tao HW, Zhang LI. A feedforward inhibitory circuit mediates lateral refinement of sensory representation in upper layer 2/3 of mouse primary auditory cortex. J. Neurosci. 2014; 34:13670–13683. [PubMed: 25297094]

Meng X, Kao JP, Kanold PO. Differential signaling to subplate neurons by spatially specific silent synapses in developing auditory cortex. J. Neurosci. 2014; 34:8855–8864. [PubMed: 24966385]

Petrus E, Isaiah A, Jones AP, Li D, Wang H, Lee HK, Kanold PO. Crossmodal induction of thalamocortical potentiation leads to enhanced information processing in the auditory cortex. Neuron. 2014; 81:664–673. [PubMed: 24507197]

Petrus E, Rodriguez G, Patterson R, Connor B, Kanold PO, Lee HK. Vision Loss Shifts the Balance of Feedforward and Intracortical Circuits in Opposite Directions in Mouse Primary Auditory and Visual Cortices. J. Neurosci. 2015; 35:8790–8801. [PubMed: 26063913]

Röder B, Teder-Sälejärvi W, Sterr A, Rösler F, Hillyard SA, Neville HJ. Improved auditory spatial tuning in blind humans. Nature. 1999; 400:162–166. [PubMed: 10408442]

Rose HJ, Metherate R. Auditory thalamocortical transmission is reliable and temporally precise. J. Neurophysiol. 2005; 94:2019–2030. [PubMed: 15928054]

Rothschild G, Nelken I, Mizrahi A. Functional organization and population dynamics in the mouse primary auditory cortex. Nat. Neurosci. 2010; 13:353–360. [PubMed: 20118927]

Schroeder CE, Foxe J. Multisensory contributions to low-level, ‘unisensory’ processing. Curr. Opin. Neurobiol. 2005; 15:454–458. [PubMed: 16019202]

Shepherd GM, Pologruto TA, Svoboda K. Circuit analysis of experience-dependent plasticity in the developing rat barrel cortex. Neuron. 2003; 38:277–289. [PubMed: 12718861]

Suter BA, O'Connor T, Iyer V, Petreanu LT, Hooks BM, Kiritani T, Svoboda K, Shepherd GM. Ephus: multipurpose data acquisition software for neuroscience experiments. Front. Neural Circuits. 2010; 4:100. [PubMed: 21960959]

Vakulin A, Catcheside PG, Baulk SD, Antic NA, van den Heuvel CJ, Banks S, McEvoy RD. Auditory evoked potentials remain abnormal after CPAP treatment in patients with severe obstructive sleep apnoea. Clin. Neurophysiol. 2012; 123:310–317. [PubMed: 21821469]

Van Boven RW, Hamilton RH, Kauffman T, Keenan JP, Pascual-Leone A. Tactile spatial resolution in blind braille readers. Neurology. 2000; 54:2230–2236. [PubMed: 10881245]

Viswanathan S, Bandyopadhyay S, Kao JP, Kanold PO. Changing microcircuits in the subplate of the developing cortex. J. Neurosci. 2012; 32:1589–1601. [PubMed: 22302801]

Winkowski DE, Kanold PO. Laminar transformation of frequency organization in auditory cortex. J. Neurosci. 2013; 33:1498–1508. [PubMed: 23345224]

Winkowski DE, Bandyopadhyay S, Shamma SA, Kanold PO. Frontal cortex activation causes rapid plasticity of auditory cortical processing. J. Neurosci. 2013; 33:18134–18148. [PubMed: 24227723]

Wu GK, Arbuckle R, Liu BH, Tao HW, Zhang LI. Lateral sharpening of cortical frequency tuning by approximately balanced inhibition. Neuron. 2008; 58:132–143. [PubMed: 18400169]

Zhao C, Kao JP, Kanold PO. Functional excitatory micro-circuits in neonatal cortex connect thalamus and layer 4. J. Neurosci. 2009; 29:15479–15488. [PubMed: 20007472]

Highlights

- Dark exposure (DE) after critical period refines circuits in auditory cortex (A1)
- DE alters intra- and inter-laminar excitatory and inhibitory circuits to L2/3 cells
- DE does not change the balance of excitation and inhibition
- Modeling shows that the altered circuits give more reliable evoked responses

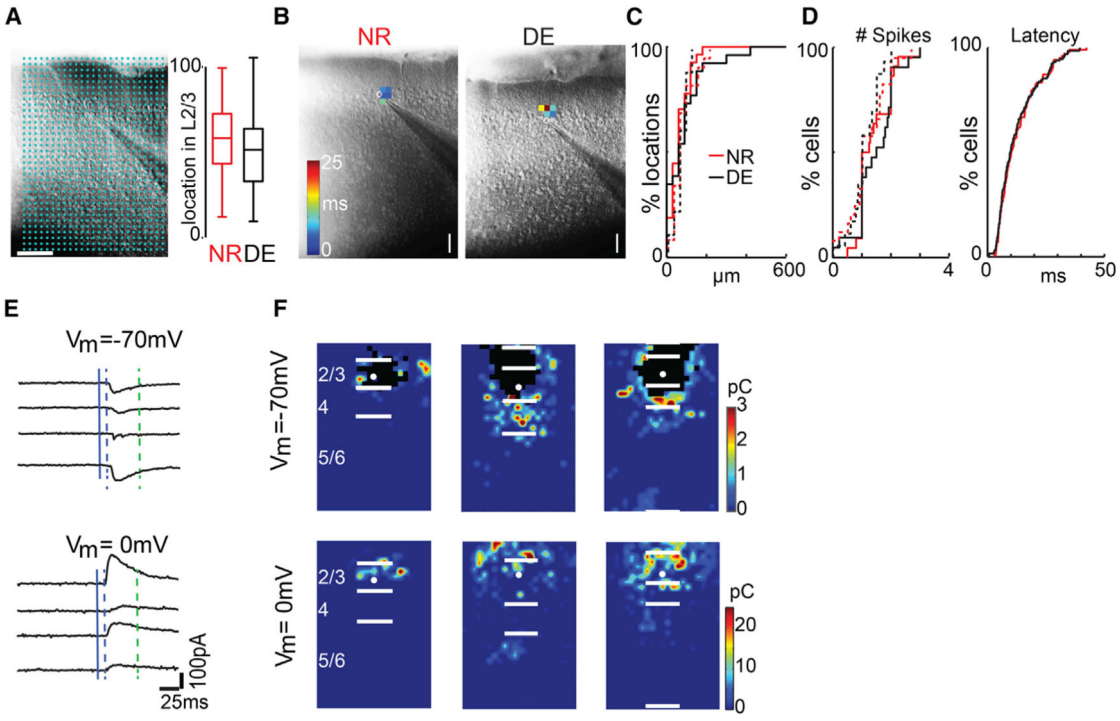

Figure 1. LSPS to Map Intracortical Connections to L2/3 Cells

(A) (Left) Infrared image of brain slice with patch pipette on layer 2/3 neuron (left). Stimulation grid is indicated by blue dots. The scale bar represents 200 µm. (Right) Position of recorded neurons within layer 2/3 is shown. Plotted is the relative position within layer 2/3 with 0 referring to the border with layer 4 and 100 referring to the border with layer 1. Cells were sampled from the middle of layer 2/3 in NR and DE animals ($p = 3.08–1$; KS test).

(B) Measurement of spatial excitability profile by cell-attached recordings combined with photostimulation. Latencies for action potentials evoked in L2/3 neurons are encoded as pseudocolor. Note that action potentials were only evoked in a restricted area around the cell body. The scale bar represents 100 µm.

(C and D) Distribution of distance within which 80% action potentials evoked over the population of neurons in L2/3 (C, solid line; n = 27 NR; n = 26 DE) and L4 (C, dashed line; n = 27 NR; n = 26 DE), number of evoked action potentials (D, left graph; L2/3: solid line; L4: dashed line), and latency distribution of action potentials evoked in L2/3 neurons (D, right). Note that most spikes were evoked within 100 µm. The spatial excitation profiles (L2/3: $p = 0.928$; L4: $p = 0.890$; KS test) and numbers of evoked action potentials (L2/3: $p = 0.731$; L4: $p = 0.660$; KS test) of L2/3 and L4 neurons and latency distribution of L2/3 neurons ($p = 0.996$; KS test) were similar.

(E) Whole-cell voltage clamp recordings at holding potentials of –70 mV (top left) or 0 mV (top right) distinguish between photostimulation-evoked excitatory and inhibitory currents. Shown are traces obtained with photostimulation at different locations. Solid blue line indicates time of photostimulation; dashed blue line marks 8-ms post-stimulus, which is the minimal latency for synaptic responses; and dashed green line marks 50 ms, the end of the analysis window.

(F) Pseudocolor maps show PSC charge at each stimulus location for three cells. Direct responses indicated were set to zero. White filled circle marks the soma location. Horizontal bars indicate layer borders. Note that, although the maps can be diverse, most cells received input from within L2/3 and L4.

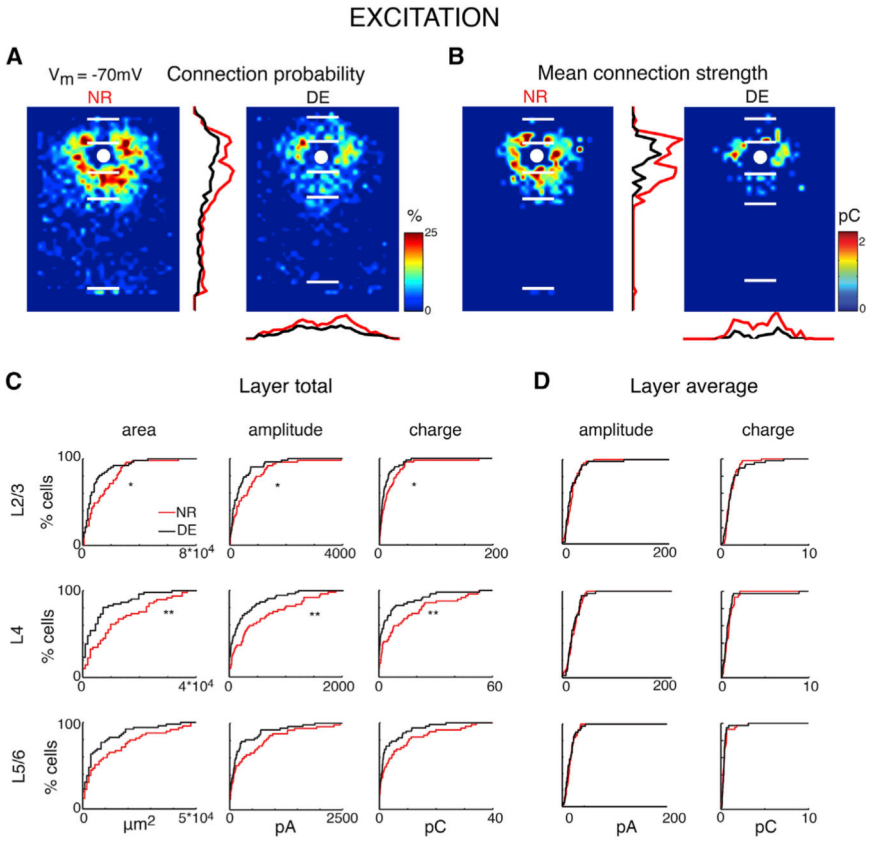

Figure 2. Excitatory Input Maps to L2/3 Neurons Are Changed after DE

(A) Average maps (aligned to soma, white circle) of connection probability for excitatory connections in NR (left) and DE (right) animals. Connection probability is encoded according to the pseudocolor scale. White horizontal lines indicate averaged laminar borders and are 200 μm long. Traces in the center show the laminar marginal distributions (red for NR and black for DE). Traces at the bottom of the DE panel indicate the columnar marginal distributions. Note that NR and DE maps and distributions appear different.

(B) Average maps (aligned to soma, white circle) of connection strength (transferred charge) for excitatory inputs in NR (left) and DE (right) animals. Averages are only calculated for stimulation sites that evoked responses in >10% of cells in our sample. Connection strength is encoded according to the pseudocolor scale. White horizontal lines indicate averaged laminar borders and are 200 μm long. Traces in the center show the laminar marginal distributions (red for NR and black for DE). Traces at the bottom of the DE panel indicate the columnar marginal distributions. Note that NR and DE maps and distributions appear different.

(C) Distributions of area of input (left), total EPSC input amplitude (center), and total EPSC input charge (right) originating from L2/3 (top), L4 (middle), and L5/6 (bottom) of NR (red) or DE (black) animals. Significance: * denotes $p < 0.05$; ** denotes $p < 0.01$. EPSC area distributions: L2/3: $p = 0.0218$; L4: $p = 0.000782$; L5/6: $p = 0.0518$. Total EPSC amplitude distributions: L2/3: $p = 0.04.91$; L4: $p = 0.00351$; L5/6: $p = 0.0891$. Total EPSC charge distributions: L2/3: $p = 0.0491$; L4: $p = 0.0040$; L5/6: $p = 0.0652$. All comparisons were done with a KS test.

(D) Distributions of average EPSC amplitude (left) and average EPSC charge (right) originating from L2/3 (top), L4 (middle), and L5/6 (bottom) for cells from NR (red) or DE (black) animals. All $p > 0.05$. Average EPSC amplitudes distributions: L2/3: $p = 0.364$; L4: $p = 0.869$; L5/6: $p = 0.551$. Average EPSC charge distributions: L2/3: $p = 0.910$; L4: $p = 0.918$; L5/6 $p = 0.644$. All comparisons were done with a KS test.

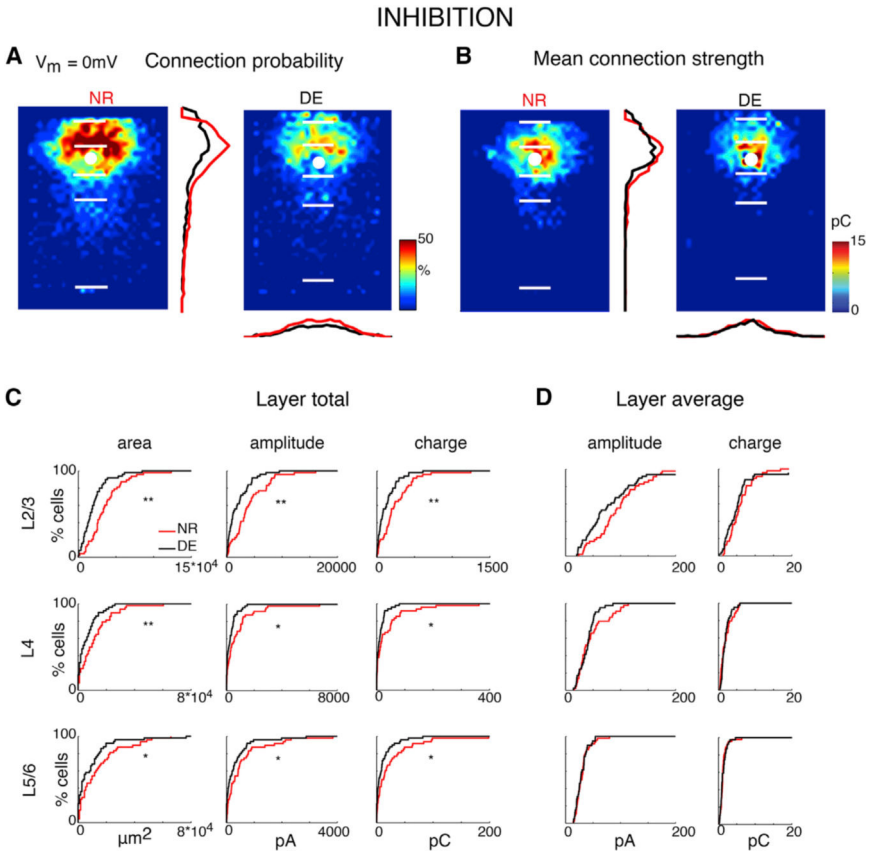

Figure 3. Inhibitory Input Maps to L2/3 Neurons Are Changed after DE

(A) Average maps (aligned to soma, white circle) of connection probability for inhibitory inputs in NR (left) and DE (right) animals. Connection probability is encoded in pseudocolor. White horizontal lines indicate averaged laminar borders and are 200 µm long. Traces in the center show the laminar marginal distributions (red for NR and black for DE). Traces at the bottom of the DE panel indicate the columnar marginal distributions. Note that NR and DE maps and distributions appear different.

(B) Average maps (aligned to soma, white circle) of connection strength (transferred charge) for inhibitory connections in NR (left) and DE (right) animals. Averages are only calculated for stimulation sites that evoked responses in >10% of cells in our sample. Connection strength is encoded in pseudocolor. White horizontal lines indicate averaged laminar borders and are 200 µm long. Traces in the center show the laminar marginal distributions (red for NR and black for DE). Traces at the bottom of the DE panel indicate the columnar marginal distributions. Note that NR and DE maps and distributions appear different.

(C) Distributions of area of input (left), total IPSC input amplitude (center), and total IPSC input charge (right) originating from L2/3 (top), L4 (middle), and L5/6 (bottom) of NR (red) or DE (black) animals. Significance: * denotes $p < 0.05$; ** denotes $p < 0.01$. IPSC area distributions: L2/3: $p = 0.000324$; L4: $p = 0.00969$; L5/6: $p = 0.020$. Total IPSC amplitude distributions: L2/3: $p = 0.000663$; L4: $p = 0.0137$; L5/6: $p = 0.0234$. Total IPSC charge distributions: L2/3: 0.00172; L4: 0.0303; L5/6: 0.0191. All comparisons were done with a KS test.

(D) Distributions of IPSC amplitude (left) and IPSC charge (right) originating from L2/3 (top), L4 (middle), and L5/6 (bottom) of NR (red) or DE (black) animals. All $p > 0.05$. Average IPSC amplitude distribution: L2/3: $p = 0.850$; L4: $p = 0.105$; L5/6: $p = 0.559$. Average IPSC charge: L2/3: $p = 0.816$; L4: $p = 0.710$; L5/6: $p = 0.854$. All comparisons were performed with a KS test.

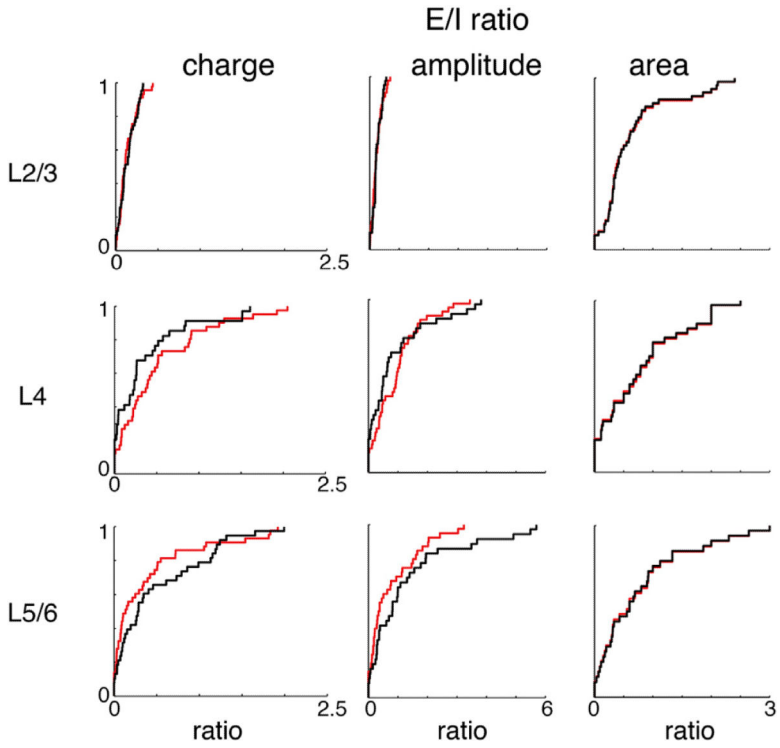

Figure 4. The Balance of Excitation and Inhibition Does Not Change after DE

Cumulative distributions (CDFs) of EI charge ratio (left), amplitude ration (middle), and area (right) from L2/3 (top), L4 (middle), and L5/6 (bottom) in NR and DE cells. No differences were observed between NR and DE (EI charge ratio: L2/3: p = 0.966; L4: p = 0.213; L5/6: p = 0.464. EI amplitude ratio: L2/3: p = 0.977; L4: p = 0.139; L5/6: p = 0.360. EI area ratio: L2/3: p = 1; L4: p = 0.979; L5/6: p = 1). All comparisons were done with a KS test.

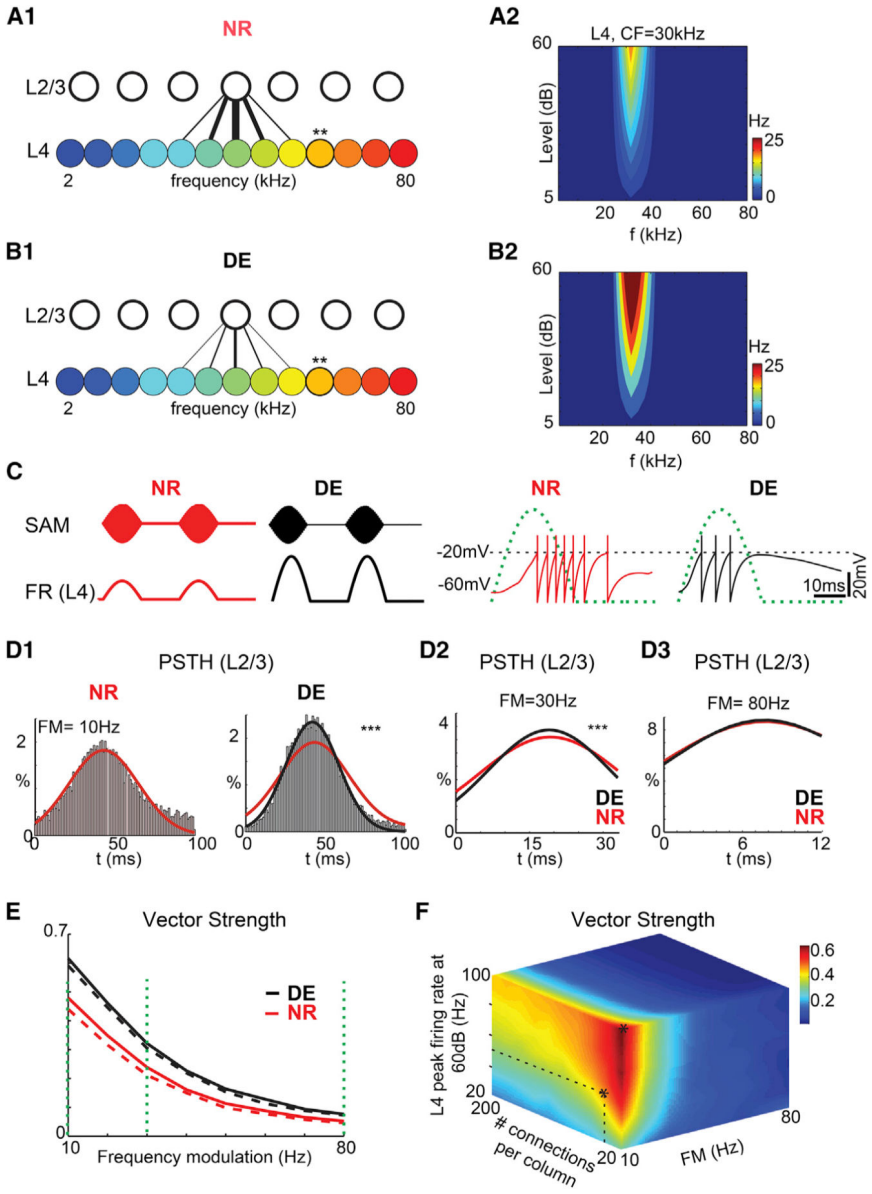

Figure 5. Circuit Changes after DE Can Enhance Sound Encoding

(A) Network diagrams of the auditory model in NR case. (A1) The regions of the auditory models (L4 and L2/3) form a network of feed-forward connections. The connection strength is represented by the thickness of lines. (A2) Frequency response map from a L4 neuron is shown (indicated by "**" in A1).

(B) Network diagrams of the auditory model in DE case. (B1) After DE, connections from L4 to L2/3 refine (also see Figure 2). (B2) After DE, connections from thalamus to L4 strengthen (Petrus et al., 2014) while the average connection strength from L4 to L2/3 stays constant (Figure 4).

(C) (Left) Rectified sinusoidal amplitude-modulated (SAM) tone stimuli (top traces; carrier frequency is 1 kHz and modulation frequency is 20 Hz) and modulated firing rates (FR) in L4 neurons (lower traces). (Right) Membrane voltage (V_m) from a L2/3 unit is shown (solid

red and black traces). Horizontal dashed line shows the threshold for triggering a spike. Green dashed waveform indicates the SAM stimulus.

(D) Post-stimulus time histograms (PSTH) of a single L2/3 unit for different frequency modulation values (10 Hz, 30 Hz, and 80 Hz). (D1) PSTH for NR (left) and DE (right) at 10 Hz is shown. Solid curves are Gaussian fits to spike distributions NR (red) and DE (black). The NR Gaussian (red) is reproduced on the DE histogram to aid visual comparison. The vector strength reflects the width of the temporal distribution over which spikes occur. Note that, for this example, spikes are distributed over a smaller time interval in DE than in NR (the width of the Gaussian fit for NR spike distribution is 25.26 ± 0.98 [95% confidence interval], whereas it is 20.06 ± 0.47 in DE; $p = 1.66 \times 10^{-104}$; F test), reflected in smaller vector strength for the NR condition. (D2 and D3) PSTH distributions for NR and DE for 30 Hz and 80 Hz modulation are shown. The DE distribution is narrower for 30 Hz modulation ($p = 0.000203$; F test), but not 80 Hz ($p = 0.45$; F test).

(E) Vector strength as function of modulation frequency, with L4 peak firing rate at 50 Hz (NR, red) and 100 Hz (DE, black) and the number of connections per column from L4 to L2/3 units being 20 (NR, red) and 10 (DE, black). Vector strength decreases with modulation frequency. Note that DE enhances vector strength over a large range even with a doubled spontaneous firing rate of L4 neurons (NR, dashed red line; DE, dashed black line). Vertical dashed lines indicate the modulation frequencies for the distributions in (D1)–(D3).

(F) Results of parametric variation of L4 firing rate and connection divergence. Vector strength increases for a large range of combinations.